Groundwater flow through continuous permafrost along geological boundary revealed by electrical resistivity tomography

Hornum Mikkel Toft[1], Betlem Peter[2], and Hodson Andrew[2]

[1]University of Copenhagen
[2]The University Centre in Svalbard

November 16, 2022

Abstract

In continuous permafrost regions, pathways for transport of sub-permafrost groundwater to the surface sometimes perforate the frozen ground and result in the formation of a pingo. Explanations offered for the locations of such pathways have so far included hydraulically conductive geological units and faults. On Svalbard, several pingos locate at valley flanks where these controls are apparently lacking. Intrigued by this observation, we elucidated the geological setting around such a pingo with electrical resistivity tomography. The inverted resistivity models showed a considerable contrast between the uphill and valley-sides of the pingo. We conclude that this contrast reflects a geological boundary between low-permeable marine sediments and consolidated strata. Groundwater presumably flows towards the pingo spring through glacially induced fractures in the strata immediately below the marine sediments. Our finding suggests that flanks of uplifted Arctic valleys deserve attention as possible discharge locations for deep groundwater and greenhouse gasses to the surface.

Groundwater flow through continuous permafrost along geological boundary revealed by electrical resistivity tomography

Mikkel Toft Hornum[1,2], Peter Betlem[1,3], and Andy Hodson[1,4]

[1]Department of Arctic Geology, The University Centre in Svalbard, N-9171 Longyearbyen, Svalbard, Norway, [2]Department of Geosciences and Natural Resource Management, and Center for Permafrost, University of Copenhagen, 1350 Copenhagen K, Denmark, [3]Department of Geosciences, University of Oslo, Sem Sælands Vei 1, N-0371 Oslo, Norway, [4]Department of Environmental Science, Western Norway University of Applied Sciences, Røyrgata 6, N-6856 Sogndal, Norway.

Corresponding author: Mikkel Toft Hornum (mth@ign.ku.dk)

Key Points:

- Electrical resistivity surveys link the location of a pingo spring to the transition between marine valley sediments and consolidated strata
- Groundwater flow towards the pingo spring most likely follows glacially induced fractures in consolidated strata produced during glaciation
- Flanks of uplifted Arctic valleys deserve attention as discharge locations for sub-permafrost groundwater and dissolved greenhouse gasses

Abstract

In continuous permafrost regions, pathways for transport of sub-permafrost groundwater to the surface sometimes perforate the frozen ground and result in the formation of a pingo. Explanations offered for the locations of such pathways have so far included hydraulically conductive geological units and faults. On Svalbard, several pingos locate at valley flanks where these controls are apparently lacking. Intrigued by this observation, we elucidated the geological setting around such a pingo with electrical resistivity tomography. The inverted resistivity models showed a considerable contrast between the uphill and valley-sides of the pingo. We conclude that this contrast reflects a geological boundary between low-permeable marine sediments and consolidated strata. Groundwater presumably flows towards the pingo spring through glacially induced fractures in the strata immediately below the marine sediments. Our finding suggests that flanks of uplifted Arctic valleys deserve attention as possible discharge locations for deep groundwater and greenhouse gasses to the surface.

1 Introduction

In continuous permafrost regions, several deep (sub-permafrost) groundwater systems have shown to be artesian and to host considerable amounts of methane and carbon dioxide (Hodson et al., 2019, 2020; Huq et al., 2017). Continuous permafrost separates deep groundwater and other fluids from the atmosphere, but exchange to and from shallower depths may still take place if taliks (i.e., locally unfrozen ground) perforate the frozen ground (i.e., a through-talik). In a warming climate, permafrost thaw alters the hydrogeological conditions, and transfer rates of methane, CO_2 and other substances are expected to increase (Grosse et al., 2016; Schuster et al., 2018). We need to understand the present hydrological setting in order to quantify the potential impact of anthropogenic global warming upon fluid migration in the Arctic,

Perennial springs in the High Arctic exemplify through-taliks that carry groundwater (hereafter 'active through-taliks') towards the ground surface (Andersen et al., 2002; Grasby et al., 2012; Haldorsen et al., 1996; Williams, 1970). A pingo (i.e., an ice-cored hill) forms when this spring discharge freezes below the thaw-protecting active layer (Mackay, 1998). By definition, this pingo will be of the open-system type because it is fed by groundwater not enclosed by permafrost (Liestøl, 1996). Pingos persist for as long as permafrost conditions remain, and even so after the through-talik has potentially frozen over and the spring discharge has ceased. Consequently, open-system pingos indicate current or previous presence of active through-taliks (Yoshikawa, 2013).

Both active through-taliks and open-system pingos require artesian pressure in the sub-permafrost groundwater system (French, 2017). In areas of continuous permafrost, such pressures may be produced by recharge from glacial meltwater infiltrating the ground below warm-based glaciers (e.g., Liestøl, 1977; Scheidegger & Bense, 2014) or, where permafrost is relatively young, by freezing expansion associated with basal permafrost aggradation (Hornum et al., 2020). While artesian pressure is a prerequisite for the transport of deep groundwater towards the surface, a sufficiently hydraulically conductive pathway is also needed. Permeable geological units (e.g., Haldorsen et al., 1996) and faults (e.g., Rossi et al., 2018; Scheidegger et al., 2012; Scholz & Baumann, 1997; Z. Wu et al., 2005) comprise the current examples of such migration pathways.

In Svalbard, many pingos are found along valley flanks (Humlum et al., 2003), and several of these occur where no links to hydraulically conductive geological units or faults are known (Ballantyne, 2018). We propose that that a combination of low-permeability Holocene marine sediments and underlying fractures resulting from pre-Holocene glacial loading and unloading may constitute a previously overseen explanation for springs located at valley margins. Figure 1 illustrates our conceptual model for spring formation at valley margins with cross-sections of the side of a typical glacially-cut valley on Svalbard ranging from glaciation to present day conditions. During the various glaciation cycles, glacial loading and unloading has caused ground compression and decompression along with fracturing (Figure 1a–b; e.g., Neuzil, 2012). Glacial fracturing of the subsurface is likely most abundant within the valleys, because of the greater pressures generated here (Leith et al., 2014a, 2014b). Following deglaciation, low-permeability marine and deltaic sediments are deposited on top of the fracture zone (Gilbert et al., 2018), confining groundwater flow (Figure 1c). Given the right conditions, a spring forms at the end of the hill slope (Figure 1d, Fitts, 2002) when the sea retreats. In Late Holocene, temperatures drop to form continuous permafrost (Humlum, 2005; Mangerud & Svendsen, 2017), but the ground stays unfrozen below the spring site due to hydrological advective heat transfer (Figure 1e). As permafrost thickness increases, the active through-talik forms along the fractured zone, because it comprises the most hydraulically conductive pathway (Figure 1f).

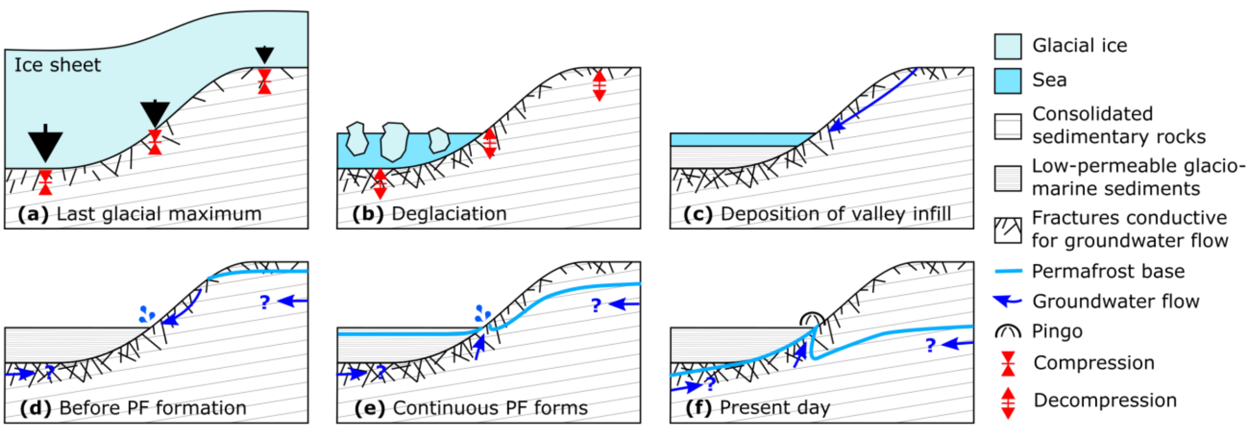

Figure 1 Cross sections of a typical valley on Svalbard showing our conceptual model of why many pingos locate at valley margins (Figure 2). **a)** and **b)** Glacial loading (a) and unloading (b), respectively, causes compression and decompression of the ground and results in fracturing (Leith et al., 2014a, 2014b). The fractures produced this way are more abundant below valley bottoms. **c)** Low-permeable marine and deltaic sediments are deposited in the fjord valley (Gilbert et al., 2018) constituting and low-permeable cover on top of the conductive fracture zone. **d)** After relative sea-level fall, a spring forms at the end of hill slope. **e)** Continuous permafrost forms, but the ground stays unfrozen below the spring site due to advective heat transfer. **f)** Comprising the most hydraulically conductive pathway, groundwater is transported towards the spring along the fractured layer.

Surface-based electrical methods have been widely used to map and characterize frozen and unfrozen ground in permafrost environments (Kneisel et al., 2008). In most locations, frozen ground can be expected to have a significantly higher electrical resistivity (>1000 Ωm, Kneisel & Hauck, 2008) than unfrozen (<500 Ωm, Palacky, 1988). However, clay-rich and saline permafrost environments may possess significantly lower resistivities. Frozen clay and other fine-grained sediments can host microfilms of unfrozen water even at temperatures below -5 °C (Scott et al., 1990) and show electrical resistivities below 100 Ωm (Harada & Yoshikawa, 1996; Keating et al., 2018; Minsley et al., 2012). Upon ground freezing, groundwater brinification may take place as solutes are expelled to the residual water (Cochand et al., 2019). Saline, unfrozen, and electrically conductive groundwater may occur as microfilms within frozen ground (Keating et al., 2018) or as larger inclusions (i.e., cryopegs; Gilbert et al., 2019; Gilichinsky et al., 2003).

We investigate the above conceptual model by elucidating the geological and hydrogeological context at the margins of a valley-flank, active open-system pingo by measuring the electrical resistivity in the ground.

2 Study site

The study site was Førstehytte Pingo (FHP), one of five open-system pingos in Lower Adventdalen, found in central Spitsbergen, the biggest island in the Svalbard archipelago (Figure 2a). As for the rest of Svalbard, continuous permafrost dominates Adventdalen due to a cold and dry climate. Permafrost thicknesses range from <200 m in the valley floor to >450 m in the adjacent mountains (Christiansen et al., 2005; Humlum et al., 2003; Liestøl, 1977). With one exception, all five pingos are active and perennially discharge brackish methane-rich waters in orders of 10^{-1} L s^{-1} (Hodson et al., 2019, 2020; Hornum et al., 2020; Liestøl, 1977; Yoshikawa, 1993; Yoshikawa & Nakamura, 1996). The chemistry of the spring discharge shows that all pingos relate to a regional sub-permafrost groundwater system (Hodson et al., 2020; Hornum et al., 2020). The two most up-valley pingos, Innerhytte (IHP) and River (RP) pingos, have formed in fractured shale and their positions are likely explained by an underlying fault that constitutes a hydraulically conductive pathway (Figure 2a, Rossi et al., 2018). Moving westwards into the lowest part of Adventdalen, FHP is the first of three pingos (the other two being Longyear, LYRP, and Lagoon, LP, pingos) that all have formed in Holocene marine muds (Yoshikawa & Harada, 1995), but locate close to the boundary to well-consolidated sedimentary rock (Figure 2b). All three align with the Northeastern flank of Adventdalen and the elongated shapes of LP and FHP are both parallel with this alignment.

Below the valley floor of Adventdalen, an up 60 m thick succession of Late Weichselian to Holocene glacio-marine and deltaic sediments overlies well-consolidated rocks of Cretaceous age or older (Figure 2, Gilbert et al., 2018). Together, all units comprise a groundwater system with a very low permeability, and most fluid flow is restricted to fractures in the consolidated bedrock. Such fractures are found in particular stratigraphic units (Figure 2b, Olaussen et al., 2020, and references therein) and in the consolidated sedimentary rock immediately below glacio-marine succession (Figure 2b, Gilbert et al., 2018). Fractures in the latter are likely of glaciogenic origin (e.g., Neuzil, 2012).

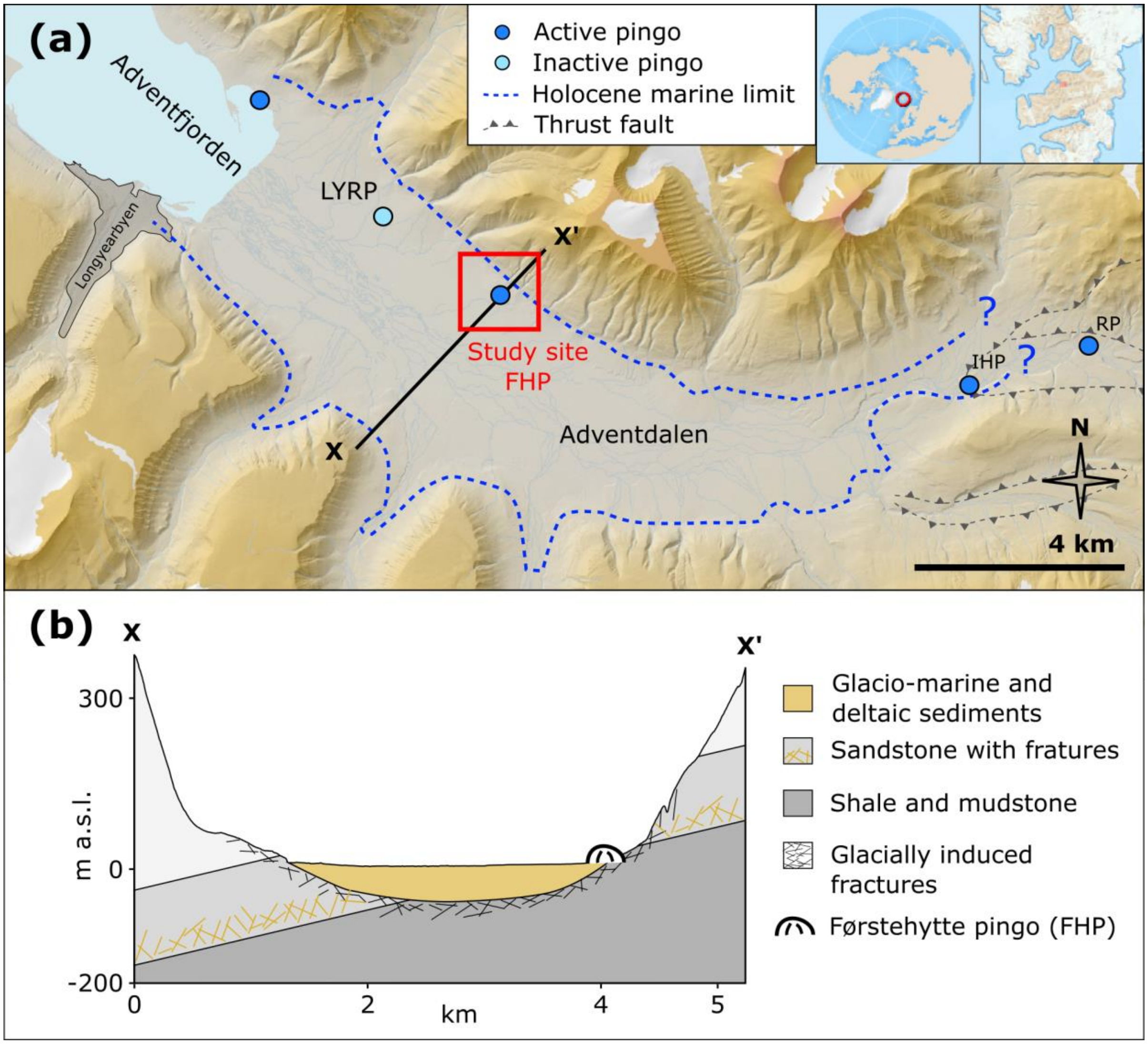

Figure 2 a) Overview of Lower Adventdalen that shows the location of pingos, the study site (red square), and the Holocene marine limit. Topographic data used to create the map by courtesy of Norwegian Polar Institute (2020). **b)** Geological cross-section across Adventdalen and the study site. Fractures in the sandstone unit and below the succession of glacio-marine and deltaic sediments interrupt the dominant low-permeability of the groundwater system. Cross-section modified from Hodson et al., 2020).

3 ERT - Data collection and processing

Measurements of direct current (DC) resistivity in the ground below FHP were carried out along four 2D transects through electrical resistivity tomography (ERT) surveying implementing the Wenner-α configuration (cf., Reynolds, 2011) during three weeks in September 2017 (Figure 3). At this time of year, the thawed active layer allowed for easy installation of electrodes and good electrical connectivity with the ground. The ERT surveys were performed with an ABEM-SAS-1000 Terrameter coupled with an ABEM-ES10-64 Electrode Selector. The layout for a single survey consisted of four cables in a roll-along configuration, each with 21 electrode take-outs and an electrode spacing of 5 m. Only uneven electrode take-outs were used and the last takeout on a cable was aligned with the first takeout on the subsequent one so that the combined cable was 400 m long and connected to 41 stainless steel electrodes. All possible four-electrode Wenner-α configurations were measured in both normal and reciprocal mode to reduce measurement error (Binley & Kemna, 2005; Kim et al., 2016). This resulted in 260 unique electrode configurations and a maximum of 520 measurements for each line. Less measurements were available when electrodes were left out due to bad connectivity to the ground. The current induced to the ground varied between 200–1000 mA. Thirteen surveys were carried out along the four transects covering most of the pingo margin (Figure 3). At each transect, two to four surveys were undertaken and provided ca. 300 m overlap between consecutive surveys. This resulted in total transect lengths of 500, 600 or 700 m, respectively comprising 375, 490 and 605 unique electrode configurations.

Electrode positions were mapped with a handheld GPS device (Garmin GPSMAP® 76C). When measuring the coordinate position within a limited time (<1 hr), this device showed to have a relatively high precision (<0.1 m) but low accuracy (<2 m). We adjusted for the low accuracy by noting particular electrodes, whose locations could be accurately pinpointed on the orthomap (Figure 3) and translated the coordinates accordingly. Because of the relatively poor vertical precision of handheld GPS measurements, we inferred the topography along the ERT lines by projecting the electrode positions on a 5-m-resolution DEM of the field area (not shown, Norwegian Polar Institute, 2020).

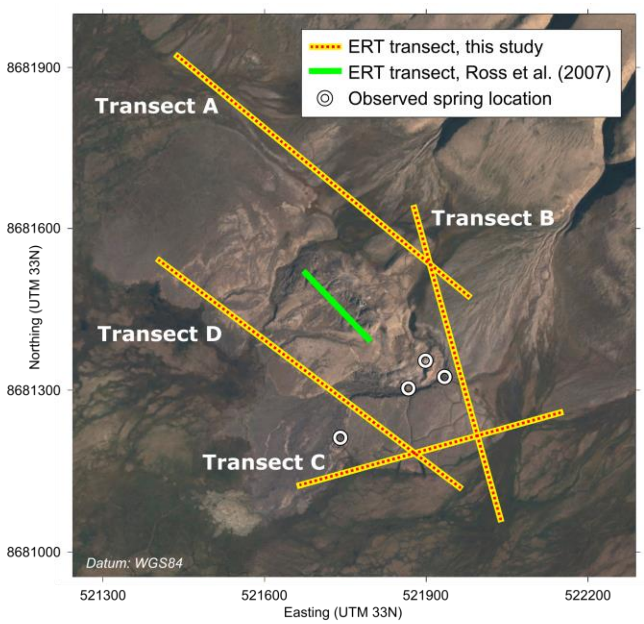

Figure 3 Orthophoto of the study site at Førstehytte Pingo showing the location of the four ERT transects from this study, the ERT transect from Ross et al. (2007) and observed spring locations. The location of the study site is shown on Figure 2. Orthophoto by courtesy of Norwegian Polar Institute (2020).

To ensure good quality of the resistivity data used for the inversion, we first performed statistical data cleaning. The final product of this pre-processing was four files, one for each transect, containing up to one measurement for each unique electrode configuration. Details of the data pre-processing can be found in the Supporting Information (Text S1).

2D inversion of the measured apparent resistivities were carried out using the graphical user interface (GUI) of ResIPy 3.0.1, an open-source software for inversion and modelling of geoelectrical data (Blanchy et al., 2020). ResIPy builds on the R2 code (version 4.02, Binley, 2019) for the inversion of DC resistivities. We employed a triangular mesh for the inversion. Following the default settings in the GUI of ResIPy, the mesh was composed of a fine mesh that defined the region of the final resistivity model encompassed by a coarse mesh. The lateral extent of the fine mesh was the transect length and the coarse mesh extended five times the transect length to both sides. The fine-to-coarse mesh boundary was at 50 m b.g.l. and the coarse mesh extended to a depth of 30% the total lateral mesh extent. The resolution of the fine mesh was defined by a characteristic length of 4.38 and a growth factor of 4. This resulted in fine meshes with 1705, 1490, 1582 and 1741 triangles for transects A, B, C and D, respectively. We used the inversion type ‘normal regularization with linear filtering’ and the convergence criterion was defined by a root-mean-square error (RMSE) of <1.2%. The certainty of the electrical resistivities predicted by the inversion was quantified by sensitivity maps as calculated by the default settings in ResIPy (Eq. 5.19 in Binley & Kemna, 2005). Sensitivity values below unity indicate that inverted resistivities are weakly constrained by data. Similarly, higher values indicate that inverted resistivities are well constrained by data and allows for greater faith in the resistivity model.

All measured and inverted electrical resistivity data resulting from this research is public available from the Zenodo repository (Hornum, 2021).

4 Results

Figure 4 shows the electrical resistivity models produced by the inversion of the measured values and the sensitivity of the resistivity values predicted by these models. To facilitate further spatial understanding, we also produced a 3D animation. In addition to the resistivity models produced from our own survey, the animation also shows a resistivity model from FHP presented by Ross et al. (2007). The animation is available as Supporting Information (Movie S1).

The electrical resistivity models predicted significantly varying values and patterns at different sides of FHP. Based on the differences of the predicted resistivity values, we divided the transects into three segments (I, II, and III), which are summarized in Table 1 and described in detail below.

Segment I covers transects A, B, and the eastern part of Transect C and situate between FHP and the mountainside. The resistivity model show that the subsurface here generally is characterized by high resistivity values that range from 1000 to 5000 Ωm. Relatively large and elongated zones up to ~200 x 60 m (width x height) of very high resistivities (5000–50000 Ωm) are also common, but these do not extend to depths shallower than ~10 m b.g.l.

Segment II possesses the most complex resistivity pattern of this survey. This segment locates south of the southeastern end of FHP and covers the western part of Transect C and the southeastern part of Transect D. In approximately the deepest 15 to 25 m, Segment II is characterized by low resistivity values that range from 20 to 100 Ωm. A relatively sharp boundary (<5 m) marks the transition to a lateral zone of moderate to high resistivity values (500–5000 Ωm). This resistivity range generally dominates the shallowest 25–35 m of the subsurface, but not at the boundary to Segment II (Transect C), where low resistivity values extent to near the surface. The moderate to high resistivities are distributed in a heterogeneous way, and vary between the extreme ends of the range several times along the extent of Segment II.

Moving on to Segment III and the southwestern flank of FHP, a further decrease in the ground resistivity can be observed. Segment III covers the northwestern part of the Transect D and locates between FHP and the valley center. Low resistivity values of up to 50 Ωm characterize the lower part of Segment III and gradually decrease upwards to very low resistivity values of down to 1.8 Ωm. A sharp boundary can be observed in the shallow part of Segment III towards Segment II in the form of the contrasting resistivities, but at greater depths the resistivity values are close to identical in both segments.

Showing mostly logarithmic values above zero, the sensitivity maps on Figure 4 indicate that the majority of the inverted resistivity values are relatively well constrained by the measurements. The sensitivity map of Segment III forms an exception to this pattern by showing log-sensitivity values below zero except for in the shallowest cells. The predicted resistivities in Segment III were thus generally not well constrained by the measurements.

Table 1 Summary of electrical resistivity patterns observed on the resistivity models (Figure 4).

	Segment A	**Segment B**	**Segment C**
Transects	A, B, C (E*)	C (W*), D (SE*)	D (NW*)
Relative position	North and East of FHP.	South of southeastern end of FHP	West
Resistivity pattern	High resistivities (/) with patches of very high resistivities occurring >10 m b.g.l.	Low resistivities in the deepest 15–25 m. (/) Moderate to high resistivities in the shallowest 25–35 m distributed in a complex pattern. Low resistivities reach near the surface at the boundary to segment II.	Very low resistivities in the top gradually increasing to low resistivities at the base.
Resistivity range	1000–5000 Ωm / 5000–50000 Ωm	20–100 Ωm / 500–5000 Ωm	1.8–50 Ωm

*Compass directions in brackets indicate when only that part of transect belongs to the segment.

Figure 4 (next page) Resistivity models of ERT transects produced by the inversion with ResIPy 3.0.1 (Blanchy et al., 2020) and log-sensitivity of these resistivity models. Log-sensitivity values below zero (blue colors) indicate that the predicted resistivities are poorly constrained by the measurements while higher values (red colors) indicate better constrain. The insert at the bottom shows the location of the transects (see also Figure 3). The number of iterations and final root-mean-square error (RMSE) are written in the lower left corner of each transect. Based on the observed resistivities, we divided the transects into three segments. A description of these are summarized in Table 1.

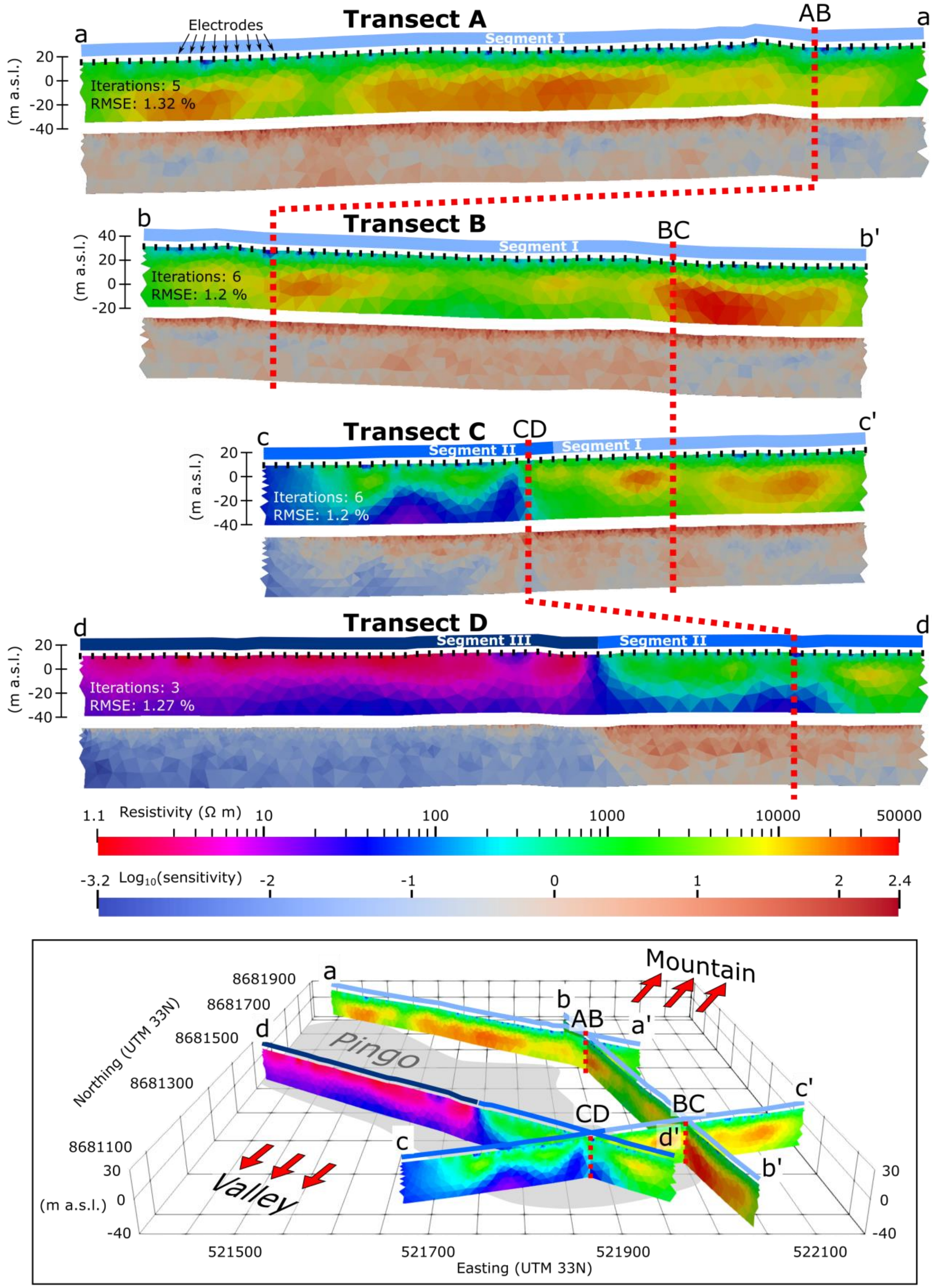

Transect A
a
a'
AB
Electrodes
Segment I
Iterations: 5
RMSE: 1.32 %
(m a.s.l.)
20
0
-20
-40
Transect B
b
b'
BC
Segment I
Iterations: 6
RMSE: 1.2 %
40
Transect C
c
c'
CD
Segment II
Segment I
Iterations: 6
RMSE: 1.2 %
Transect D
d
d'
Segment III
Segment II
Iterations: 3
RMSE: 1.27 %
Resistivity (Ω m)
1.1
10
100
1000
10000
50000
Log10(sensitivity)
-3.2
-2
-1
0
1
2
2.4
Mountain
Pingo
Valley
Northing (UTM 33N)
8681900
8681700
8681500
8681300
8681100
Easting (UTM 33N)
521500
521700
521900
522100
30
-40

242

5 Discussion - Implications of resistivity models

Indicating a robust inversion, log-sensitivity values above zero dominated the majority of the resistivity models (Figure 4) and suggested that most of the predicted values represent true ground conditions. However, the low sensitivities dominating Segment III indicated that the resistivity values predicted here should be interpreted with greater caution. When low resistivity values dominate shallow ground conditions, the depth of current flow is reduced and measurements are thus less sensitive to deeper layers of the subsurface (Binley, 2015). For Segment III, this implied that the predicted low resistivities may conceal zones of higher resistivities. To quantify this potential concealment, we conducted a series of forward modelling experiments with ResIPy, which are described in detail in the Supporting Information (Text S2). From these experiments, we conclude that low resistivities dominate at least the shallowest 15 m b.g.l. and likely extent to more than 25 m b.g.l.

The relatively strong differences observed on the resistivity models surrounding FHP (Figure 4) indicate varying conditions in the subsurface. In the following, we consider salinity, lithology and phase of state as possible explanations for these differences.

Completely unfrozen ground could not explain the low resistivities in Segment III (Figure 4), because of the known occurrence of permafrost and the fact that the low resistivities completely dominate the ground, rather than appearing as zones or patches within higher resistivity values. Instead, we attributed the low resistivities of segment III to the Holocene marine sediments of which FHP is also composed (Yoshikawa & Harada, 1995). Although such low resistivities (1.8–50 Ωm, Figure 4) would not be expected for most permafrost environments (e.g., Draebing & Eichel, 2017; Lewkowicz et al., 2011; Sjöberg et al., 2015), they are consistent with previous measurements of marine sediments in Adventdalen (Harada & Yoshikawa, 1996; Keating et al., 2018; Ross et al., 2007). Laboratory experiments of saline permafrost soils also show similar resistivities (Y. Wu et al., 2017), although the difference in scale makes this comparison less confident. We infer that an unfrozen saline water content of <5% documented in other parts of Adventdalen (Gilbert et al., 2019; Keating et al., 2018) likely also explains the low resistivities of Segment III.

The high and very high resistivities measured on the other side of FHP (Segment I, Figure 4, Table 1) did not comply with the above explanation. Instead, the modelled values (1000–50000 Ωm) pointed to permafrost with a limited unfrozen water content (Kneisel & Hauck, 2008) and as such would be difficult to explain if the ground consisted of the aforementioned marine sediments. We instead interpret the high resistivities to reflect a different lithology, which, given the geological context, is likely to be shale or mudstone (Figure 2b). The quite significant resistivity range may have resulted from differences in fracture abundance, lithological differences or differences in ground ice concentration, but borehole calibration or other investigations are needed before an unequivocal interpretation can be made.

Constituting the transition between Segments I and III, and thus two different lithologies, Segment II presumably spans a geological boundary. At the same time, this segment passes closely to recent spring locations that may affect subsurface thermal regimes and influence subsurface resistivities. As such, the moderate to high resistivities distributed heterogeneously throughout the segment are likely explained as zones with high ice concentrations. This view is consistent with ERT surveys of the internal structures of Longyear and Førstehytte Pingos that documented similar complex resistivity patterns (Ross et al., 2007). Ross et al.'s (2007) ERT survey at FHP resulted in a 175 m long profile running in a NE-SW direction along the crest of the pingo (Figure 3). We digitized this profile and present it along with our own survey results in a 3D animation, which, to our knowledge, shows all ERT transects from FHP (link to 3D animation).

As for our survey, different lithologies and groundwater salinities often characterize the ground in coastal environments. This results in electrical resistivity contrasts that may not correlate with the distribution of frozen and unfrozen ground, and interpretations of frozen and unfrozen ground state may thus be challenging. However, as this survey also shows, electrical resistivity contrasts controlled by salinity and lithology may be increased as permafrost becomes established, and electrical surveys will consequently be able to detect these contrasts more easily.

From the above interpretation, we see that FHP is located exactly at the boundary between the consolidated bedrock and the marine valley infill. Assuming that this is not a coincidental conjunction, one needs to consider the geological boundary when explaining the location of FHP. The conjunction might be explained by groundwater recharge in the adjacent highlands discharging at the foothill. However, such explanation would not be consistent with the high electrical ground resistivities found towards the mountainside. Instead, the conjunction of FHP and the geological boundary is in line with the aforementioned conceptual model (Figure 1) that glacially induced fractures in the sedimentary bedrock comprise a hydrological pathway for deep groundwater to reach the surface. This view is supported by the geochemistry of pingo spring waters in Adventdalen, which indicates a deep groundwater origin (Hodson et al., 2020; Hornum et al., 2020).

To our knowledge, no other investigation at any of the open-system pingos in Svalbard that are found along valley flanks (e.g., Humlum et al., 2003) have mapped the geological context in detail. Still, we hypothesise that a similar mechanism may also contribute to the formation of some of the open-system pingos found in Svalbard in similar geological contexts. This would readily explain for example the elongated shapes of LP and FHP and their alignment with the valley flank.

6 Conclusions

This study is the first to show a direct relationship between a geological boundary and an open-system pingo. The strong electrical resistivity contrast observed between the uphill and valley sides of Førstehytte Pingo likely reflects a lithological difference: the high resistivities observed towards the mountainside are consistent with frozen sedimentary rocks with a limited groundwater content, while permafrost with a low but saline content of groundwater explains the low resistivities on the valley-side. Groundwater presumably flows flow to the pingo springs through fractures in the sedimentary bedrock induced during glacial loading and unloading. This view is supported by spring water geochemistry that indicates a deep groundwater origin and by the consistently high electrical ground resistivities towards the mountainside of FHP, which does not favor a topographic groundwater source. The numerous pingos on Svalbard that also locate along valley margins are possibly associated with this boundary as well, and if so, these are explained by groundwater in glacial fractures. Our findings indicate that shallow fractures in the Late Weichselian landscape relief may constitute a previously overlooked groundwater pathway. The fracture zone may link deep groundwater systems to the surface, where low-permeable sediments cover this surface. On a circumpolar scale, flanks of uplifted valleys deserve particular attention as possible pathways for subsurface fluids.

Acknowledgments

This work was conducted within the Catchment Transport and Cryohydrology Network (CatchNet) funded by the Swedish Nuclear Fuel and Waste Management Company (SKB), and the CLIMAGAS project (Climate forcing of terrestrial methane gas escape through permafrost in Svalbard) funded by the Research Council of Norway (grant no. NRC 294764). The authors acknowledge Aart Kroon and Ylva Sjöberg for critical feedback and comments to an earlier version of this manuscript. For help in the field, the authors thank Matt, Linn, Trine, Antoine, Daniela, Erik and UNIS students of the AG340 course. The measured and inverted electrical resistivity data supporting this research is public available from the Zenodo repository (Hornum, 2021).

References

Andersen, D. T., Pollard, W. H., McKay, C. P., & Heldmann, J. (2002). Cold springs in permafrost on Earth and Mars. *Journal of Geophysical Research E: Planets*, *107*(3). https://doi.org/10.1029/2000je001436

Ballantyne, C. K. (2018). *Periglacial geomorphology*. Hoboken, New Jersey, USA: John Wiley & Sons Ltd.

Binley, A. (2015). Tools and Techniques: Electrical Methods. In G. Schubert (Ed.), *Treatise on Geophysics* (2nd ed., Vol. 11, pp. 233–259). Amsterdam, the Netherlands: Elsevier. https://doi.org/10.1016/B978-0-444-53802-4.00192-5

Binley, A. (2019). *R2 version 4.0 (November 2019)*. Lancaster, England: Lancaster University. Retrieved from http://www.es.lancs.ac.uk/people/amb/Freeware/R2/R2_readme.pdf

Binley, A., & Kemna, A. (2005). DC Resistivity and Induced Polarization Methods. In Y. Rubin & S. S. Hubbard (Eds.), *Hydrogeophysics* (1st ed., Vol. 50, pp. 129–156). New York, USA: Springer. https://doi.org/10.1007/1-4020-3102-5

Blanchy, G., Saneiyan, S., Boyd, J., McLachlan, P., & Binley, A. (2020). ResIPy, an intuitive open source software for complex geoelectrical inversion/modeling. *Computers and Geosciences*, *137*(104423). https://doi.org/10.1016/j.cageo.2020.104423

Christiansen, H. H., French, H. M., & Humlum, O. (2005). Permafrost in the Gruve-7 mine, Adventdalen, Svalbard. *Norsk Geografisk Tidsskrift*, *59*(2), 109–115. https://doi.org/10.1080/00291950510020592

Cochand, M., Molson, J., & Lemieux, J. M. (2019). Groundwater hydrogeochemistry in permafrost regions. *Permafrost and Periglacial Processes*, *30*(2), 90–103. https://doi.org/10.1002/ppp.1998

Draebing, D., & Eichel, J. (2017). Spatial Controls of Turf-Banked Solifluction Lobes and Their Role for Paraglacial Adjustment in Glacier Forelands. *Permafrost and Periglacial Processes*, *28*(2), 446–459. https://doi.org/10.1002/ppp.1930

Fitts, C. R. (2002). *Groundwater Science*. *Groundwater Science* (1st ed.). Cambridge, MA, USA: Academic Press. https://doi.org/10.1016/C2009-0-62950-0

French, H. M. (2017). *The Periglacial Environment* (4th ed.). Hoboken, New Jersey, USA: John Wiley & Sons Ltd.

Gilbert, G. L., O'Neill, H. B., Nemec, W., Thiel, C., Christiansen, H. H., & Buylaert, J. P. (2018). Late Quaternary sedimentation and permafrost development in a Svalbard fjord-valley, Norwegian high Arctic. *Sedimentology*, *65*(7), 2531–2558. https://doi.org/10.1111/sed.12476

Gilbert, G. L., Instanes, A., O. Sinitsyn, A., & Aalberg, A. (2019). Characterization of two sites for geotechnical testing in permafrost: Longyearbyen, Svalbard. *AIMS Geosciences*, *5*(4), 868–885. https://doi.org/10.3934/geosci.2019.4.868

Gilichinsky, D., Rivkina, E., Shcherbakova, V., Laurinavichuis, K., & Tiedje, J. (2003). Supercooled water brines within permafrost - An unknown ecological niche for microorganisms: A model for astrobiology. *Astrobiology*, *3*(2), 331–341. https://doi.org/10.1089/153110703769016424

Grasby, S. E., Beauchamp, B., & Bense, V. (2012). Sulfuric acid speleogenesis associated with a glacially driven groundwater system-paleo-spring "pipes" at Borup Fiord Pass, Nunavut. *Astrobiology*, *12*(1), 19–28. https://doi.org/10.1089/ast.2011.0700

Grosse, G., Goetz, S., McGuire, A. D., Romanovsky, V. E., & Schuur, E. A. G. (2016). Changing permafrost in a warming world and feedbacks to the Earth system. *Environmental Research Letters*, *11*, 040201. https://doi.org/10.1088/1748-9326/11/4/040201

Haldorsen, S., Heim, M., & Lauritzen, S. E. (1996). Subpermafrost Groundwater, Western Svalbard. *Nordic Hydrology*, *27*(1–2), 57–68. https://doi.org/10.2166/nh.1996.0019

Harada, K., & Yoshikawa, K. (1996). Permafrost age and thickness near Adventfjorden, Spitsbergen. *Polar Geography*, *20*(4), 267–281. https://doi.org/10.1080/10889379609377607

Hodson, A., Nowak, A., Redeker, K. R., Holmlund, E. S., Christiansen, H. H., & Turchyn, A. V. (2019). Seasonal dynamics of methane and carbon dioxide evasion from an open system pingo: Lagoon pingo, svalbard. *Frontiers in Earth Science*, *7*, 30. https://doi.org/10.3389/feart.2019.00030

Hodson, A., Nowak, A., Hornum, M. T., Senger, K., Redeker, K. R., Christiansen, H. H., et al. (2020). Sub-permafrost methane seepage from open-system pingos in Svalbard. *The Cryosphere*, *14*, 3829–3842. https://doi.org/10.5194/tc-14-3829-2020

Hornum, M. T. (2021). ERT data from Førstehytte Pingo, Adventdalen, Svalbard. Zenodo. https://doi.org/DOI: 10.5281/zenodo.4479529

Hornum, M. T., Hodson, A., Jessen, S., Bense, V., & Senger, K. (2020). Numerical modelling of permafrost spring discharge and open-system pingo formation induced by basal permafrost aggradation. *The Cryosphere*, *14*, 4627–4651. https://doi.org/https://doi.org/10.5194/tc-14-4627-2020

Humlum, O. (2005). Holocene permafrost aggradation in Svalbard. *Geological Society Special Publication*, *242*, 119–130. https://doi.org/10.1144/GSL.SP.2005.242.01.11

Humlum, O., Instanes, A., & Sollid, J. L. (2003). Permafrost in Svalbard: A review of research history, climatic background and engineering challenges. *Polar Research*, *22*(2), 191–215. https://doi.org/10.3402/polar.v22i2.6455

Huq, F., Smalley, P. C., Mørkved, P. T., Johansen, I., Yarushina, V., & Johansen, H. (2017). The

Longyearbyen CO2 Lab: Fluid communication in reservoir and caprock. *International Journal of Greenhouse Gas Control*, *63*, 59–76. https://doi.org/10.1016/j.ijggc.2017.05.005

Keating, K., Binley, A., Bense, V., Van Dam, R. L., & Christiansen, H. H. (2018). Combined Geophysical Measurements Provide Evidence for Unfrozen Water in Permafrost in the Adventdalen Valley in Svalbard. *Geophysical Research Letters*, *45*(15), 7606–7614. https://doi.org/10.1029/2017GL076508

Kim, J. H., Supper, R., Ottowitz, D., Jochum, B., & Yi, M. J. (2016). A new measurement protocol of direct current resistivity data. *Geophysics*, *81*(2), A7–A11. https://doi.org/10.1190/GEO2015-0419.1

Kneisel, C., & Hauck, C. (2008). Electrical methods. In C. Hauck & C. Kneisel (Eds.), *Applied Geophysics in Periglacial Environments* (1st ed., pp. 3–27). Cambridge, England: Cambridge University Press.

Kneisel, C., Hauck, C., Fortier, R., & Moorman, B. (2008). Advances in Geophysical Methods for Permafrost Investigations. *Permafrost and Periglacial Processes*, *19*, 157–178. https://doi.org/10.1002/ppp.616

Leith, K., Moore, J. R., Amann, F., & Loew, S. (2014a). In situ stress control on microcrack generation and macroscopic extensional fracture in exhuming bedrock. *Journal of Geophysical Research: Solid Earth*, *119*(1), 594–615. https://doi.org/10.1002/2012JB009801

Leith, K., Moore, J. R., Amann, F., & Loew, S. (2014b). Subglacial extensional fracture development and implications for Alpine Valley evolution. *Journal of Geophysical Research: Earth Surface*, *119*(1), 62–81. https://doi.org/10.1002/2012JF002691

Lewkowicz, A. G., Etzelmüller, B., & Smith, S. L. (2011). Characteristics of discontinuous permafrost based on ground temperature measurements and electrical resistivity tomography, Southern Yukon, Canada. *Permafrost and Periglacial Processes*, *22*(4), 320–342. https://doi.org/10.1002/ppp.703

Liestøl, O. (1977). Pingos, springs, and permafrost in Spitsbergen. In A. Brekke (Ed.), *Norsk Polarinstitutt Årbok 1975* (pp. 7–29). Oslo, Norway: Universitetsforlaget.

Liestøl, O. (1996). Open-system pingos in Spitsbergen. *Norsk Geografisk Tidsskrift*, *50*, 81–84. https://doi.org/10.1080/00291959608552355

Mackay, J. R. (1998). Pingo growth and collapse, Tuktoyaktuk Peninsula area, western arctic coast, Canada: A long-term field study. *Geographie Physique et Quaternaire*, *52*(3), 271–323. https://doi.org/10.7202/004847ar

Mangerud, J., & Svendsen, J. I. (2017). The Holocene Thermal Maximum around Svalbard, Arctic North Atlantic; molluscs show early and exceptional warmth. *The Holocene*, *28*(1), 65–83. https://doi.org/10.1177/0959683617715701

Minsley, B. J., Abraham, J. D., Smith, B. D., Cannia, J. C., Voss, C. I., Jorgenson, M. T., et al. (2012). Airborne electromagnetic imaging of discontinuous permafrost. *Geophysical Research Letters*, *39*(L02503). https://doi.org/10.1029/2011GL050079

Neuzil, C. E. (2012). Hydromechanical effects of continental glaciation on groundwater systems. *Geofluids*, *12*(1), 22–37. https://doi.org/10.1111/j.1468-8123.2011.00347.x

Norwegian Polar Institute. (2020). Map data. Retrieved May 13, 2020, from https://geodata.npolar.no/

Olaussen, S., Senger, K., Braathen, A., Grundvåg, S.-A., & Mørk, A. (2020). You learn as long as you drill; research synthesis from the Longyearbyen CO2 Laboratory, Svalbard, Norway. *Norwegian Journal of Geology*, *99*(2), 157–187. https://doi.org/10.17850/njg008

Palacky, G. J. (1988). Resistivity Characteristics of Geologic Targets. In M. N. Nabighian (Ed.), *Electromagnetic Methods in Applied Geophysics* (Vol. 1: Theory, pp. 52–129). Tulsa, Oklahoma: Society of Exploration Geophysicists. https://doi.org/10.1190/1.9781560802631.ch3

Reynolds, J. M. (2011). *An Introduction to Applied and Environmental Geophysics* (2nd ed.). Hoboken, New Jersey, USA: John Wiley & Sons.

Ross, N., Brabham, P. J., Harris, C., & Christiansen, H. H. (2007). Internal structure of open system pingos, adventdalen, svalbard: The use of resistivity tomography to assess ground-ice conditions. *Journal of Environmental and Engineering Geophysics*, *12*(1), 113–126. https://doi.org/10.2113/JEEG12.1.113

Rossi, G., Accaino, F., Boaga, J., Petronio, L., Romeo, R., & Wheeler, W. (2018). Seismic survey on an open pingo system in Adventdalen Valley, Spitsbergen, Svalbard. *Near Surface Geophysics*, *16*(1), 89–103. https://doi.org/10.3997/1873-0604.2017037

Scheidegger, J. M., & Bense, V. F. (2014). Impacts of glacially recharged groundwater flow systems on talik evolution. *Journal of Geophysical Research: Earth Surface*, *119*(4), 758–778. https://doi.org/10.1002/2013JF002894

Scheidegger, J. M., Bense, V. F., & Grasby, S. E. (2012). Transient nature of Arctic spring systems driven by subglacial meltwater. *Geophysical Research Letters*, *39*(12), 1–6. https://doi.org/10.1029/2012GL051445

Scholz, H., & Baumann, M. (1997). An ’open system pingo’near Kangerlussuaq (Søndre Strømfjord), West Greenland. *Geology of Greenland Survey Bulletin*, *176*, 104–108. https://doi.org/https://doi.org/10.34194/ggub.v176.5074

Schuster, P. F., Schaefer, K. M., Aiken, G. R., Antweiler, R. C., Dewild, J. F., Gryziec, J. D., et al. (2018). Permafrost Stores a Globally Significant Amount of Mercury. *Geophysical Research Letters*, *45*(3), 1463–1471. https://doi.org/10.1002/2017GL075571

Scott, W. J., Sellmann, P. V., & Hunter, J. A. (1990). Geophysics in the Study of Permafrost. In S. H. Ward (Ed.), *Geotechnical and Environmental Geophysics* (Vol. 1, pp. 355–384). Tulsa, Oklahoma: Society of Exploration Geophysicists. https://doi.org/https://doi.org/10.1190/1.9781560802785.ch13

Sjöberg, Y., Marklund, P., Pettersson, R., & Lyon, S. W. (2015). Geophysical mapping of palsa peatland permafrost. *Cryosphere*, *9*(2), 465–478. https://doi.org/10.5194/tc-9-465-2015

Williams, J. R. (1970). *Ground Water in the Permafrost Regions of Alaska*. *USGS Professional Paper 696*. Reston, Virginia, USA. https://doi.org/https://doi.org/10.3133/pp696

Wu, Y., Nakagawa, S., Kneafsey, T. J., Dafflon, B., & Hubbard, S. (2017). Electrical and seismic response of saline permafrost soil during freeze - Thaw transition. *Journal of Applied Geophysics*, *146*, 16–26. https://doi.org/10.1016/j.jappgeo.2017.08.008

Wu, Z., Barosh, P. J., Hu, D., Wu, Z., Peisheng, Y., Qisheng, L., & Chunjing, Z. (2005). Migrating pingos in the permafrost region of the Tibetan Plateau, China and their hazard along the Golmud-Lhasa railway. *Engineering Geology*, *79*, 267–287. https://doi.org/10.1016/j.enggeo.2005.02.003

Yoshikawa, K. (1993). Notes on open-system pingo ice, Adventdalen, Spitsbergen. *Permafrost and Periglacial Processes*, *4*(4), 327–334. https://doi.org/10.1002/ppp.3430040405

Yoshikawa, K. (2013). Pingos. In J. Shroder, R. Giardino, & J. Harbor (Eds.), *Treatise on Geomorphology* (Vol. 8, pp. 274–297). San Diego, California, USA: Academic Press. https://doi.org/10.1016/B978-0-12-374739-6.00212-8

Yoshikawa, K., & Harada, K. (1995). Observations on nearshore pingo growth, Adventdalen, Spitsbergen. *Permafrost and Periglacial Processes*, *6*(4), 361–372. https://doi.org/10.1002/ppp.3430060407

Yoshikawa, K., & Nakamura, T. (1996). Pingo growth ages in the delta area, Adventdalen, Spitsbergen. *Polar Record*, *32*(183), 347–352. https://doi.org/10.1017/S0032247400067565

Geophysical Research Letters

Supporting Information for

Groundwater flow through continuous permafrost along geological boundary revealed by electrical resistivity tomography

Mikkel Toft Hornum[1,2], Peter Betlem[1,3], and Andy Hodson[1,4]

[1]Department of Arctic Geology, The University Centre in Svalbard, N-9171 Longyearbyen, Svalbard, Norway, [2]Department of Geosciences and Natural Resource Management, and Center for Permafrost, University of Copenhagen, 1350 Copenhagen K, Denmark, [3]Department of Geosciences, University of Oslo, Sem Sælands Vei 1, N-0371 Oslo, Norway, [4]Department of Environmental Science, Western Norway University of Applied Sciences, Røyrgata 6, N-6856 Sogndal, Norway.

Corresponding author: Mikkel Toft Hornum (mth@ign.ku.dk)

Contents of this file

Additional Supporting Information (Files uploaded separately)

Text S1. Quality check and pre-processing of measured ERT data

Prior to the inverse modelling of the measured electrical resistivities with ResIPy 3.0.0 (Blanchy et al., 2020), we performed quality checks and data cleaning to ensure a more accurate final resistivity image. During the field experiments, measured resistivity data was stored on the device (ABEM SAS-1000 Terrameter) in a binary file format (.SK4). Using the instrument specific software Terrameter SAS4000/SAS1000 Utilities (Guideline Geo AB, Stockholm), data files was retrieved from the instrument and converted to ASCII text files. In accordance with the desired input for ResIPy, the final product of the pre-processing was four files, one for each Transect, containing the unique electrode configurations and one transfer resistance value for each of these configurations (i.e., 'protocol.dat'-format; Binley, 2019). Whenever several measurements were available for the same electrode configuration (data point), we chose the statistically most significant ones and used the mean as input for the inverse modelling. Table S1 provides a numeric overview of the pre-processing and data cleaning, while a description is given in the following.

Merging of files and removal of non-reciprocal measurements

Measurements from the same run-along profile were merged into one file and the electrode numbers corrected accordingly. Empty measurements and measurements with no reciprocity were discarded leaving only complete measurements pairs (i.e., a normal and its reciprocal measurement). Prior to further data cleaning and pre-processing, the amount of complete measurements pairs prior comprised between 87–95% of the measurements scheduled in the recording protocol (Table S1).

Removal of measurements with high error (normal vs. reciprocal measurements)

The transfer resistance misfit was calculated for each measurement pair, and those with errors greater than 5% were discarded. Of the remaining measurement pairs, those with errors greater than three standard deviations were also removed (Figure S1). After the removal of these measurements, 83–91% of the scheduled measurements remained. The location of unique data points and the number of measurements pairs for each of these are plotted on Figure S2, which shows that 87–93 % of the unique data points scheduled in the measurement protocol were covered after the removal of measurements with high error. Root-mean-square errors (RMSE) of the remaining measurement pairs between 0.4–1.2% quantifies the data quality (Figure S1).

Final data cleaning

The final data cleaning was based on the mean of transfer resistances of each remaining measurement pair.

Despite a relatively good agreement between normal and reciprocal measurements (as indicated by the RMSEs, Figure S1), measurement pairs from the same data point did not always agree. This is exemplified on Figure S3, which shows transfer resistances measured with the minimum electrode spacing at Transect A. From this Figure, it is obvious that some measurements deviated by showing significantly higher transfer resistance values than the remainder. These were not regarded to represent true ground conditions, and called for further data cleaning. In order to meet with this call, we consecutively performed the data cleaning steps described below.

- By plotting all measurements like on Figure S3 (not shown), we could visually infer a transfer resistance threshold of 20 Ω and discarded all measurements above this value. The only exception was for Transect C, were the threshold was defined by a transfer resistance of 27 Ω. The upper panels (a and c) of Figure S4 exemplify transfer resistances that remain after discarding those above the threshold. Further data cleaning, as described below and exemplified by Figure S5, were carried out on these measurements and resulted in the cleaned dataset, which is exemplified by the transfer resistances plotted on the lower panels (b and d) of Figure S4.

- For data points with four measurement pairs remaining, we discarded any measurements if outside the standard deviation. As exemplified by Figure S5a, this resulted in zero, one or two measurement pairs being discarded (subplot 2, 3 and 1, respectively).
- For data points with three measurement pairs remaining, we removed the most outlying measurement pair, but only if the difference to the median was more than twice the difference between the median and the third measurement pair. Thus, on subplot 1 of Figure S5b, the upper measurement pair was discarded; while on subplot 2, no measurements were discarded.
- For data points with two measurement pairs, we used a running mean, $\tilde{\mu}_n$, calculated from the mean, μ_n, of measurements a the data point, n, and the four neighboring data points at the same recording depths (n-2, n-1, n+1, and n+2). As exemplified by subplot 3 on Figure S5c, no measurements were discarded when $\tilde{\mu}_n$ was greater or smaller than both measurement pairs. When $\tilde{\mu}_n$ was between the measured transfer resistances, the measurement pair with the largest difference to $\tilde{\mu}_n$ was discarded, but only if the difference between μ_n and $\tilde{\mu}_n$ was greater than the difference between $\tilde{\mu}_n$ and the second measurement pair. Thus, on subplot 1 of Figure S5c, the measurement pair with the highest transfer resistance was discarded; whereas no measurements on subplot 2 were discarded.
- Finally, for data points with only one measurement pair, we discarded it, if the difference to the aforementioned running mean was greater than 3 Ω. This is exemplified by Figure S5d were two measurement pairs show transfer resistances that deviate more than 3 Ω from the running mean.

Text S2. Reliability of resistivity models

In this supporting text, we consider the reliability of the electrical resistivity values predicted by the resistivity models (Figure 4) by evaluating the sensitivity maps. Indicating good constrain for the inversion, log-sensitivity values above zero dominated the majority of the resistivity models and suggests that most of the predicted values represent true ground conditions. When low resistivity values dominate shallow ground conditions, the depth of current flow is reduced and measurements are thus less sensitive to deeper layers of the subsurface (Binley, 2015). This is reflected in the low sensitivity values for Segment III and the resistivity values predicted deeper than the shallowest couple of meters should thus be considered as tentative.

The shallow low resistivities imply that Segment III (Figure 4) may conceal zones of higher resistivities at greater depth. To quantify this potential concealment, we conducted a series of forward modelling experiments with ResIPy, which are described in the following. The fine mesh domain was 50 x 700 m and the mesh was defined using the same setup as for the inversion of the field measurements (Section 3). The starting (target) resistivity model consisted of two layers: a shallow layer with a low resistivity of 5 Ωm that was intended to mimic the shallow subsurface conditions of Segment III; and a deeper layer with a high resistivity of 100, 500, 1000 or 2000 Ωm. The boundary between the two layers was located at a depth of 5, 10, 15, 25 or 35 m. The synthetic measurement protocol was defined as for the field measurements (i.e. 10 m electrode spacing, Wenner-α setup and mimicking roll-along layout) resulting in 605 unique electrode configurations (similar to Transect A and D but without topography, Figure S2). Given the starting resistivity models, domain setup and measurement protocol, the forward models could be run. Two percent noise was added to the synthetic measurements to simulate scenarios that are more realistic. The synthetic measurements were then inverted—again, using the same setup as for the field measurements.

Figure S6 shows the resistivity models produced by the forward modelling experiments, and a black dashed line is drawn to indicate which scenarios are compatible with the resistivity values predicted on Segment III (Figure 4) and which are not. The experiments suggests that if ground resistivities of 500 Ωm or more are situated above 15 m b.g.l., a survey design like the one employed here would predict resistivity values higher than what is observed in Segment III. Therefore, while the low sensitivity of Segment III does not allow for a detailed interpretation of the subsurface conditions, the predicted values still show that low resistivities dominate at least the shallowest 15 m b.g.l. and likely extent to more than 25 m b.g.l.

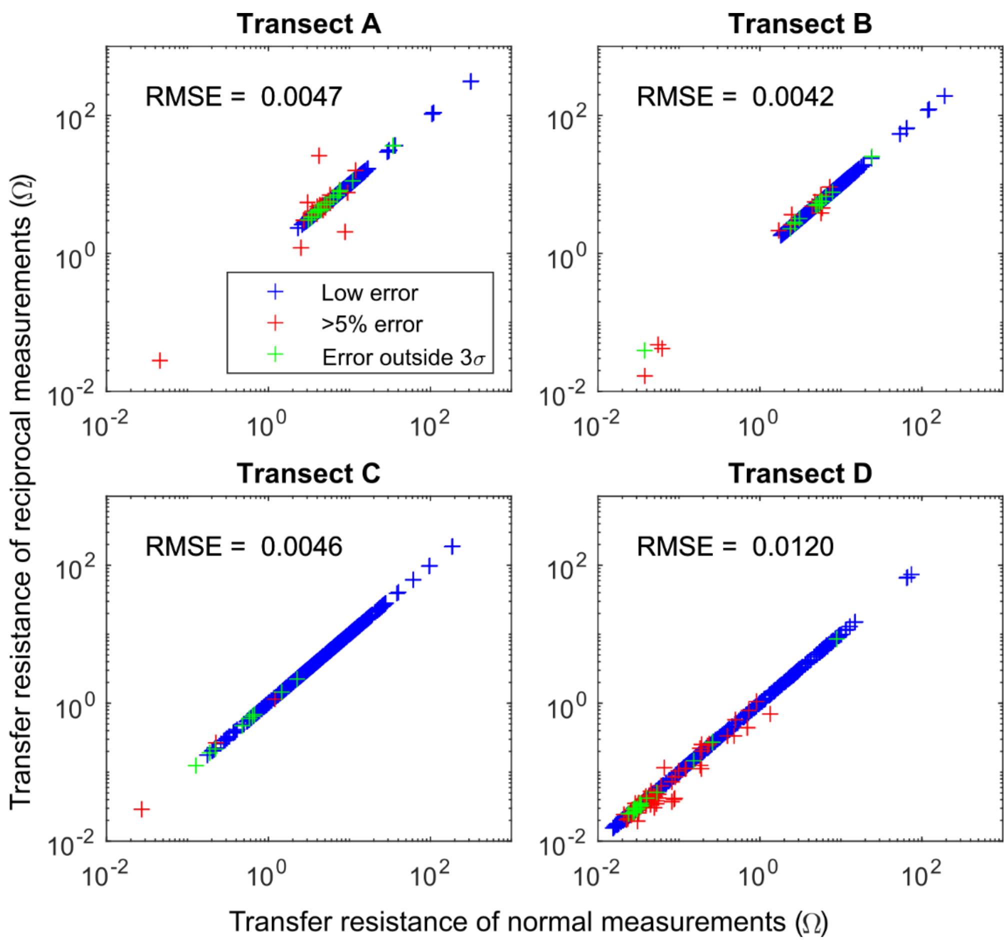

Figure S1. Transfer resistances of normal and reciprocal measurements. Measurement pairs with more than 5% error and errors outside three standard deviations (σ) were discarded. The root-mean-square errors (RMSE) are of the remaining measurements with relatively low error.

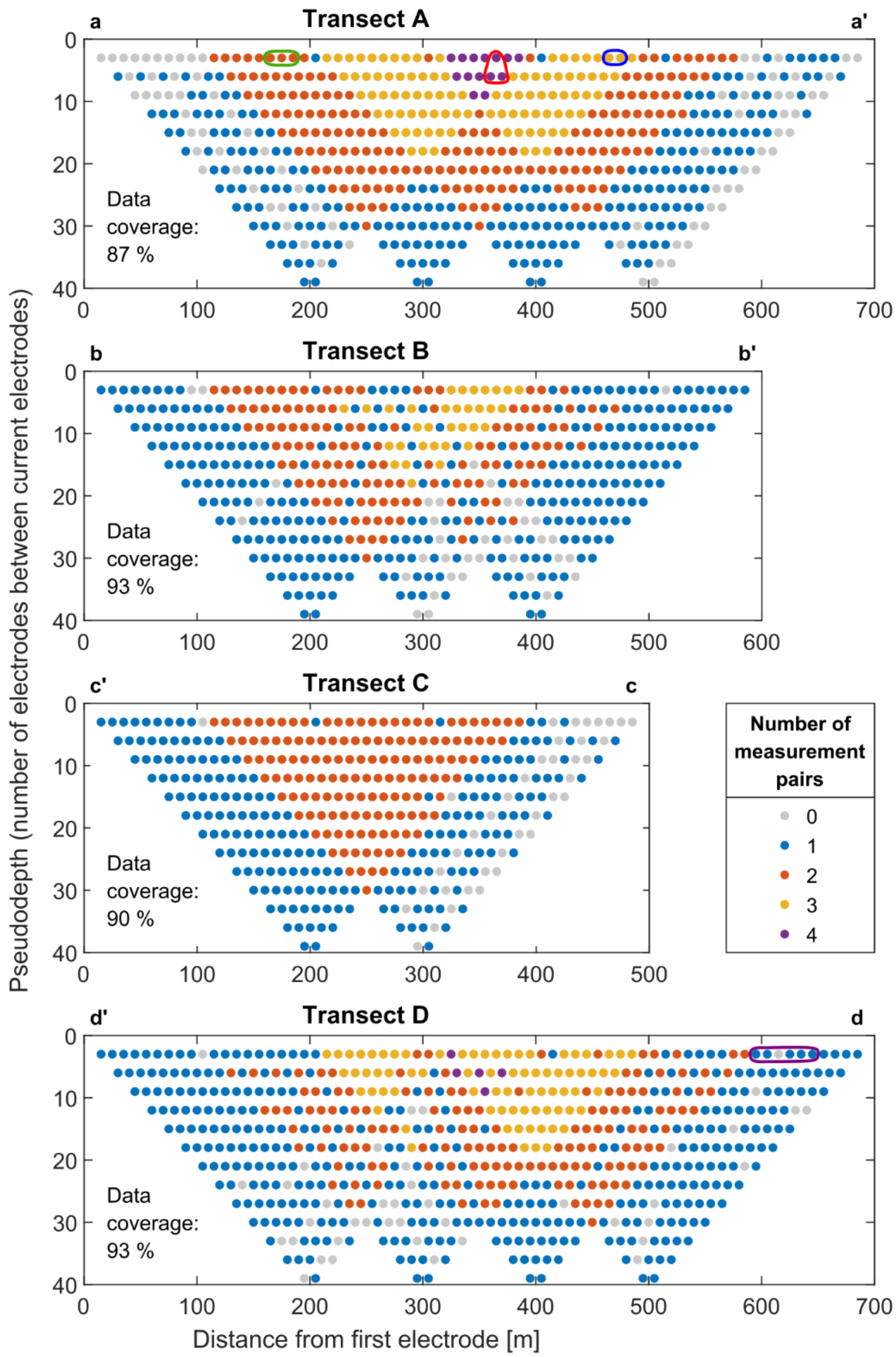

Figure S2. Overview of unique data points and number of measurement pairs remaining after removal of measurements with high error (Figure S1). Each data point correspond to a unique electrode configuration and its color indicates the number of complete measurements pairs recorded during the survey. The data coverage (lower left corner of each panel) indicates the proportion of unique data points with low error measurement pairs. Bold lowercase letters at the top of each transect indicate its orientation (see insert on Figure 3, main text). The data points surrounded by a red, blue, green or purple line are used as examples for data cleaning on Figure S5.

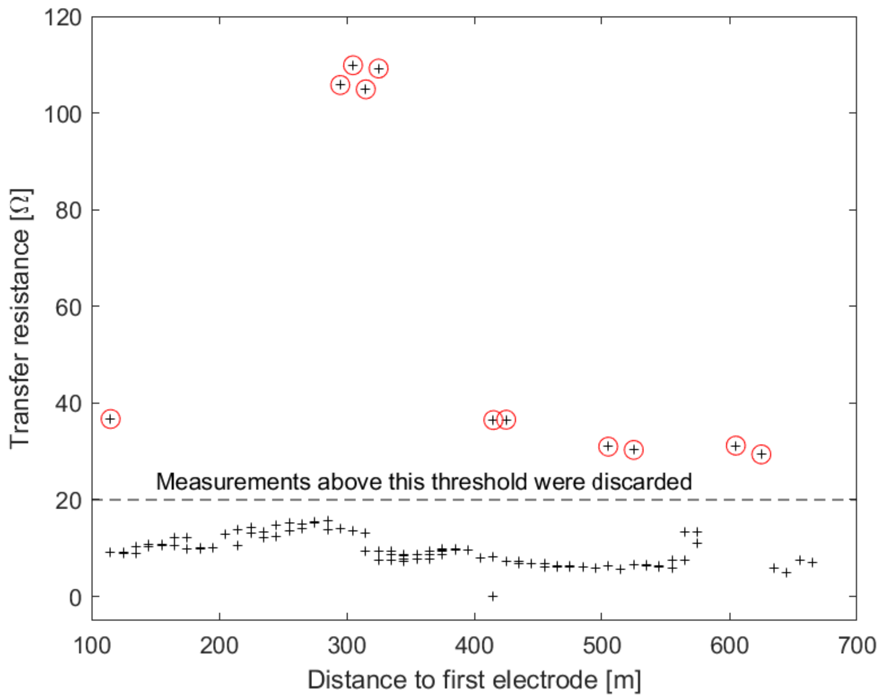

Figure S3. Transfer resistances measured with the minimum electrode spacing at Transect A. Each data point corresponds to the mean of a measurement pair. Red circles show that some measurements deviated by a considerably higher transfer resistance than the remainder. We discarded these by defining a visually interpreted upper threshold of 20Ω. Only measurement pairs with low error are included (colored data points on Figure S2).

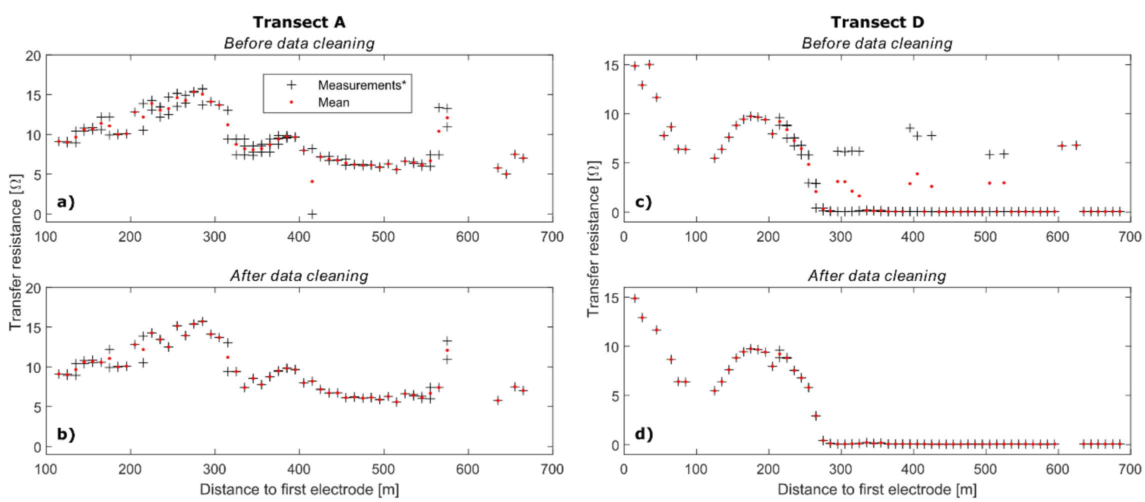

Figure S4. Transfer resistances measured with the minimum electrode spacing at Transect A (**a** and **b**) and D (**c** and **d**) before and after the final data cleaning. The upper panels, **a**) and **c**), show all measurements* that remain after the measurements above the threshold has been discarded (Figure S3). The lower panels, **b**) and **d**), show the measurements* that remain after the final data cleaning. *Black crosses correspond to the mean of a measurement pair. The mean of measurements from the same data point (i.e. same distance on the x-axis) are drawn with red dots. The red dots in the lower panels (**b** and **d**) represent the transfer resistance values used for the inverse modelling.

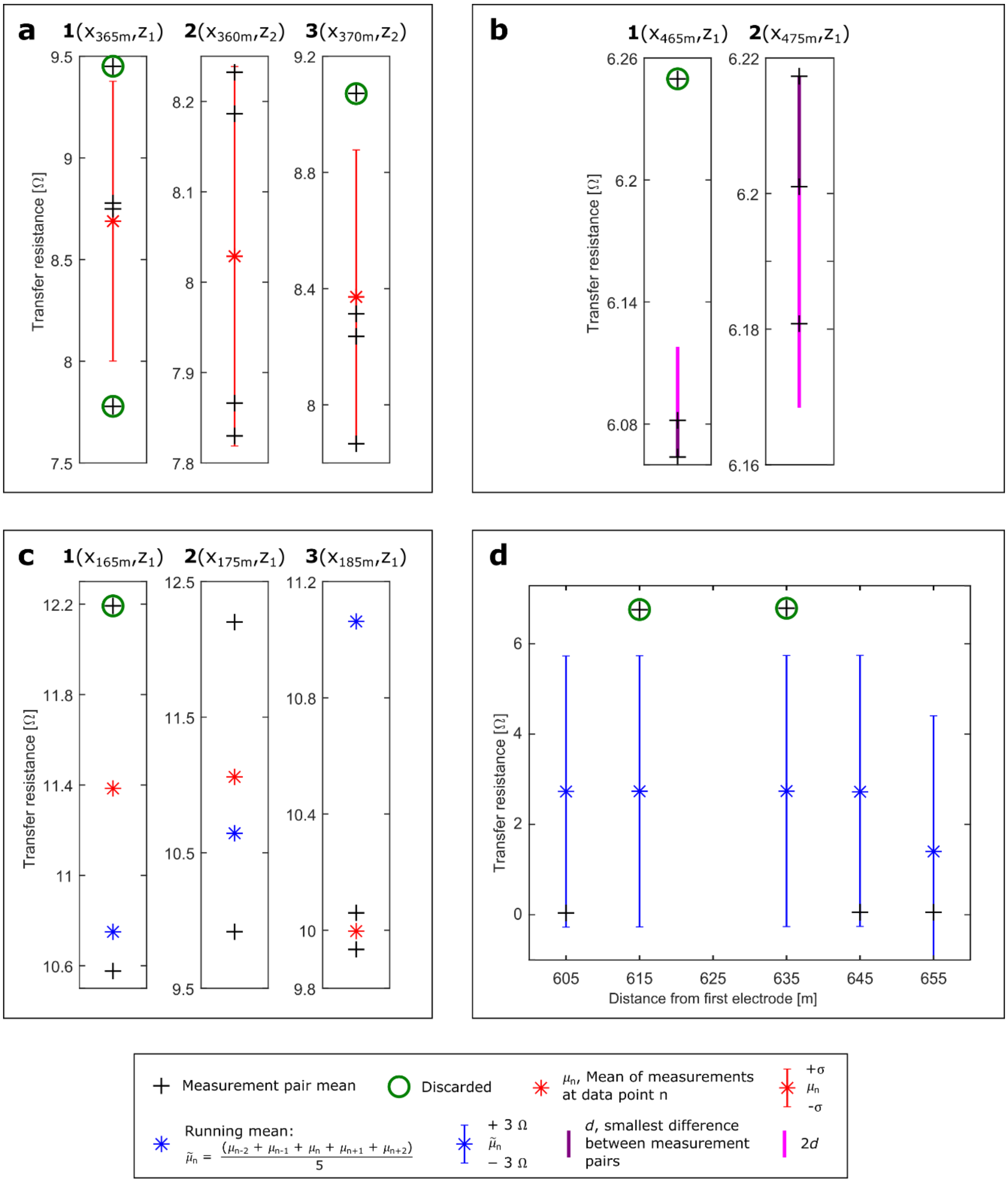

Figure S5. Examples of final data cleaning at data points with four (**a**), three (**b**), two (**c**) and one (**d**) measurements remaining after discarding measurements above the threshold (Figure S3). The examples plotted on panels **a**), **b**), and **c**) are all from Transect A, and the parenthesis on the subplot labels indicate the data point position on Transect A. The subscripts of x's are defined by the distance to the first electrode in the transect, while the subscript of z's are defined by the relative recording depth. The examples plotted on panel **d**) are all from the shallowest recording depth at Transect D. **a**) When four measurement pairs were available, measurements outside the standard deviation were discarded. As exemplified by subplots 2, 3 and 1, respectively, this procedure implied that zero, one or two measurements were removed. A red line on Figure S2 surrounds these three data points. **b**) At data points with three measurement pairs, the most outlying measurement pair was discarded if the distance to the median was more than twice the distance between the median and the third measurement. Thus, on subplot 1, the uppermost measurement pair was discarded, while on subplot 2, none were. A blue line on Figure S2 surrounds these two data points. **c**) For data cleaning at data points with two measurement pairs, we used a running mean, $\tilde{\boldsymbol{\mu}}_{\boldsymbol{n}}$, calculated from the mean, $\boldsymbol{\mu}_{\boldsymbol{n}}$, of a data point, n, and the four neighboring data points (n-2, n-1, n+1, and n+2). As exemplified by subplot 3, no measurements were discarded when $\tilde{\boldsymbol{\mu}}_{\boldsymbol{n}}$ was greater or smaller than both measurement pairs. When $\tilde{\boldsymbol{\mu}}_{\boldsymbol{n}}$ was between the measured transfer resistances, the measurement pair with the largest difference to $\tilde{\boldsymbol{\mu}}_{\boldsymbol{n}}$ was discarded, but only if the difference between $\boldsymbol{\mu}_{\boldsymbol{n}}$ and $\tilde{\boldsymbol{\mu}}_{\boldsymbol{n}}$ was greater than the difference between $\tilde{\boldsymbol{\mu}}_{\boldsymbol{n}}$ and the second measurement. This is exemplified by subplot 1, where the measurement pair with the highest transfer resistance was discarded; and by subplot 2, were no measurement was discarded. A green line on Figure S2 surrounds these three data points. **d**) Finally, for data points with only one measurement pair, we discarded it, if the difference to the running mean was greater than 3Ω. A purple line on Figure S2 surrounds the five data points plotted here.

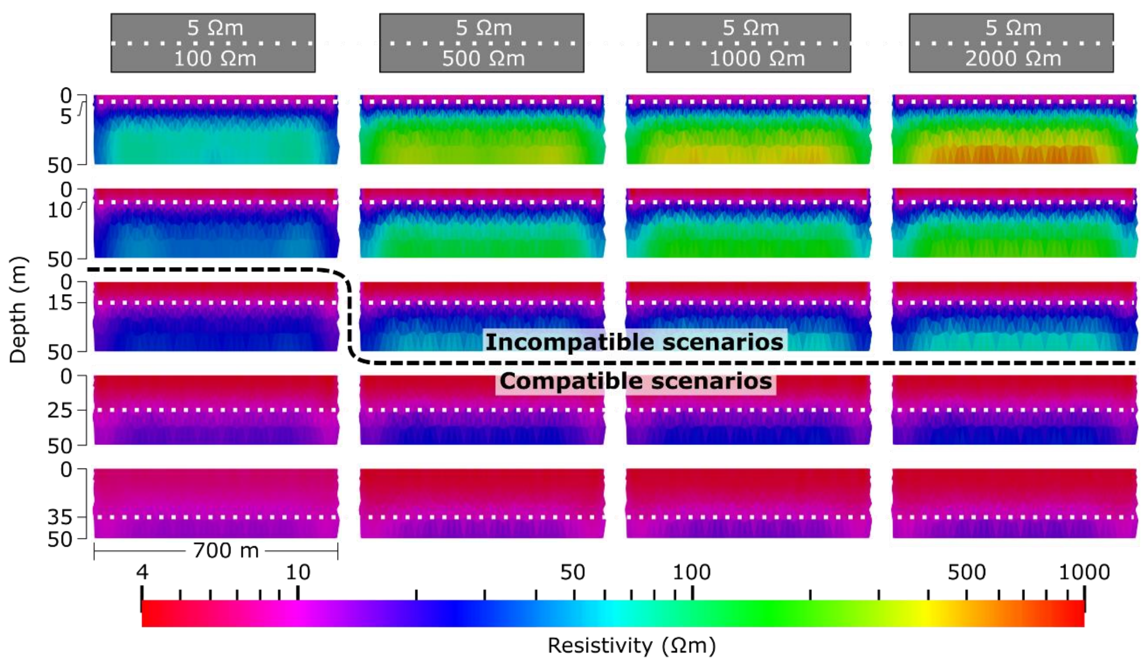

Figure S6. Resistivity models produced by forward modelling experiments intended to reveal the extent to which Segment III (Figure 4) might conceal higher resistivities than the inverted. Scenarios above the black dashed line are incompatible with Segment III, while those below are compatible. The starting models are sketched conceptually at the top of the figure: each consists of two layers, the shallow having a resistivity of 5 Ωm and the deeper a resistivity of

100, 500, 1000 or 2000 Ωm. The depth to the boundary between these two layers is indicated on the vertical axes to the left. The domain, mesh and synthetic measurement protocol was defined so that it mimics setup for the inversion of the field measurements (Section 3).

Table S1 *Summary of measured electrical resistivity data and data cleaning prior to inversion.*

Transect	**A**	**B**	**C**	**D**
Summary of initial dataset				
Number of surveys in profile	4	3	2	4
Combined length [m]	700	600	500	700
Unique electrode configurations (data point)	605	490	375	605
Number of scheduled measurement pairs	1040	780	520	1040
Not measured / no normal or reciprocal measurement	54	105	31	71
Number of complete measurement pairs	986	675	489	969
… relative to scheduled.	95%	87%	94%	93%
Data points with complete measurement pairs	551	466	344	589
Data coverage	91%	95%	92%	97%
Dataset summary after…				
… removal based on error (normal vs. reciprocal)				
Errors > 5 %	31	13	5	82
Errors > 3σ	19	15	9	16
Number of remaining measurement pairs	*936*	*647*	*475*	*871*
… relative to scheduled	*90%*	*83%*	*91%*	*84%*
Remaining data points				
Data points with one measurement	234	294	197	342
Data points with two measurements	182	127	139	142
Data points with three measurements	94	33		75
Data points with four measurements	14			5
Total number of remaining data points	524	454	336	564
Data coverage	87%	93%	90%	93%
… removal of measurements above transfer resistance threshold				
Threshold (Ω)	20	20	27	20
Measurement pairs above threshold	13	10	11	3
Remaining measurement pairs	923	637	464	868
Data points with one measurement	237	299	202	340
Data points with two measurements	182	121	131	143
Data points with three measurements	90	32		74
Data points with four measurements	13			5
Total number of remaining data points	522	452	333	562
Data coverage	86%	92%	89%	93%
… removal of measurements at data points with four measurement pairs				
Number of remaining measurements	912	637	464	863
Data points with one measurement	237	299	202	340
Data points with two measurements	182	121	131	143
Data points with three measurements	101	32		79
Data points with four measurements	2			0
Total number of remaining data points	522	452	333	562
Data coverage	86%	92%	89%	93%
… removal of measurements at data points with three measurement pairs				

Number of remaining measurements	849	610	464	802
Data points with one measurement	237	299	202	340
Data points with two measurements	245	148	131	204
Data points with three measurements	38	5		18
Data points with four measurements	2			0
Total number of remaining data points	522	452	333	562
Data coverage	86%	92%	89%	93%
… removal of measurements at data points with two measurement pairs				
Number of remaining measurements	806	574	423	768
Data points with one measurement	280	335	243	374
Data points with two measurements	202	112	90	170
Data points with three measurements	38	5		18
Data points with four measurements	2			0
Total number of remaining data points	522	452	333	562
Data coverage	86%	92%	89%	93%
… removal of measurements at data points with one measurement pair				
Number of remaining measurements	*803*	*569*	*418*	*766*
Data points with one measurement	277	330	238	372
Data points with two measurements	202	112	90	170
Data points with three measurements	38	5		18
Data points with four measurements	2			0
Total number of remaining data points	519	447	328	560
Data coverage	86%	91%	87%	93%

Table S1. Summary of measured electrical resistivity data and data cleaning prior to inversion.

Data Set S1. A zipped folder with measured and inverted ERT data from Førstehytte Pingo is public available from the Zenodo repository (Hornum, 2021). The folder has data files containing all measurements and data files with measurements remaining after data cleaning only. The latter were used for the inversion with ResIPy. In addition, inverted resistivity models and electrodes coordinates are also provided. A map of the field site provides a geographical overview. Detailed information about the deposited data files is provided in the readme file.

Movie S1. 3D animation of ERT profiles from FHP pingo. In addition to our own resistivity models, the animation also includes a profile from a survey conducted by Ross et al. (2007). Their profile locates at the crest of FHP.